PHOTONICS Research

Optical orbital angular momentum multiplexing communication via inversely-designed multiphase plane light conversion

Juncheng Fang,[1,†] Jinpei Li,[1,†] Aru Kong,[1] Youpeng Xie,[1] Chuxuan Lin,[1] Zhenwei Xie,[1,2] Ting Lei,[1,3] and Xiaocong Yuan[1,*]

[1]Nanophotonics Research Centre, Shenzhen Key Laboratory of Micro-Scale Optical Information Technology & Institute of Microscale Optoelectronics, Shenzhen University, Shenzhen 518060, China
[2]e-mail: ayst3_1415926@sina.com
[3]e-mail: leiting@szu.edu.cn
*Corresponding author: xcyuan@szu.edu.cn

Received 15 March 2022; revised 22 May 2022; accepted 12 June 2022; posted 13 June 2022 (Doc. ID 458474); published 3 August 2022

Multiplexing and demultiplexing of optical orbital angular momentum (OAM) are critical operations in mode-division multiplexing communications. Traditional Dammann gratings, spiral phase planes, and optical geometric transformations are regarded as convenient methods for OAM mode (de)multiplexing. However, crosstalk between the different modes and the difficulty of mode multiplexing greatly limit their application to mode-division multiplexing communications. Here, using a set of inversely-designed phase planes, we demonstrate an OAM (de)multiplexer based on multiphase plane light conversion that can enable perfect OAM multiplexing communication. The sorted patterns are Gaussian-like and can be coupled easily into single-mode fiber arrays. Inputs from the fiber array are turned into coaxial OAM modes after the phase planes. OAM mode crosstalk generated by the multiplexer is less than −20 dB, with insertion loss of less than 2.6 dB. OAM modes are sorted by the demultiplexer with mode crosstalk below −10 dB, and the sorting results are coupled to the fiber array. OAM modes carrying 10 Gbit/s on–off keying signals were transmitted in a 5 km few-mode fiber. The measured bit-error-rate curves have power penalties of less than 10 dB. The proposed configuration is highly efficient and convenient and will be beneficial for potential applications in quantum information, information processing, and optical communications.

https://doi.org/10.1364/PRJ.458474

1. INTRODUCTION

In 1992, Allen *et al.* revealed that an optical vortex carries orbital angular momentum (OAM) of $l\hbar$ per photon and that its wavefront is in a helical form that can be expressed as $\exp(il\varphi)$, where l is the topological charge and φ is the azimuthal angle [1,2]. Since then, OAM beams have attracted major research attention worldwide, and these beams have been used widely in optical microphotography [3–5], optical metrology [6], optical measurement applications [7], optical manipulation [8–10], and high-dimensional quantum information processing [11–15]. The orthogonality among the OAM modes provides a new degree of freedom for optical multiplexing communications [16–19]. In addition, OAM is compatible with traditional multiplexing techniques (e.g., wavelength-, time-, and polarization-division multiplexing) [16,17,20]. Because of this, OAM mode multiplexing communications have become increasingly popular in recent years. In 2012 and 2013, OAM mode multiplexing communications were demonstrated in free space and in optical fibers, respectively [21,22]. To date, however, the (de)multiplexing processes for OAM modes and, particularly, the multiplexing process remain a critical problem that prevents practical application of mode multiplexing communications. In early reports on this problem, conventional bulky optical elements were adopted for OAM generation and detection, including spatial light modulators (SLMs) [23], spiral phase planes [24], optical fork gratings or Dammann gratings [25–27], and interferometric methods [28]. In 2010, Berkhout *et al.* proposed an approach with near-perfect efficiency for free-space OAM demultiplexing based on an optical geometric transformation [29,30]. Subsequently, other researchers developed fanout and spiral transformation methods to improve the performance of this approach [31–34]. In addition, Yu *et al.* added a cylindrical lens to shape the sorted pattern into a Gaussian-like pattern [35]. After the metasurface was introduced in 2011 [36], many compact OAM (de)multiplexing devices were proposed based on this structure,

including OAM generation using geometric metasurfaces [37], OAM detection through plasmonic metasurfaces [38–41], and on-chip metagratings and inversely-designed metasurfaces for OAM (de)multiplexing [42,43]. However, these devices are not applicable to OAM (de)multiplexing communications, particularly for OAM multiplexing, because of their low sorting or mode conversion efficiencies and low compatibility between the sorted pattern and the basic mode of a single-mode fiber.

Among these OAM (de)multiplexing techniques, multi-phase plane light conversion (MPLC) [44–49], optical neural networks [50,51], and machine learning [52,53] are drawing increasing attention because of their solid performance levels and high flexibility. However, the number of phase planes required affects the practical performance, especially in terms of the mode conversion efficiency [44,49]. For symmetrical modes such as Hermit–Gaussian modes, the number of phase planes can be reduced greatly by introducing a symmetrical boundary condition [47,48]. For OAM modes, it is expected to achieve efficient and low crosstalk (de)multiplexing via inversely-designed MPLC.

In this work, we propose and demonstrate an OAM multiplexing communication technique based on MPLC that can enable perfect OAM (de)multiplexing by using a set of inversely-designed phase planes through a wavefront-matching algorithm. The proposed configuration only requires five phase planes to accomplish both OAM mode multiplexing and demultiplexing perfectly. These phase planes are fabricated on a silicon wafer using three cycles of a mask lithography procedure. The sorted pattern is a near-perfect Gaussian beam that is compatible with the base mode of a single-mode fiber and can be coupled easily into a single-mode fiber. Conversely, the light coming from a single-mode fiber array will be converted into a series of coaxial OAM modes after passing through the five phase planes. The mode conversion performed through these five optimized phase planes provides high-quality demultiplexing spots, high process efficiency, and low mode crosstalk. More importantly, the proposed configuration is both a perfect mode sorter and a perfect mode multiplexer simultaneously. In addition, the bit-error-rate (BER) curve shows that the OAM (de)multiplexer based on MPLC offers high performance for fiber communications.

2. PRINCIPLE AND MODE ANALYSIS OF INVERSELY-DESIGNED MPLC

The OAM multiplexer presented here converts multiple channels of independent input Gaussian beams into corresponding high-order coaxial OAM modes. There is no analytic function expression for inversely-designed MPLC when using the wavefront-matching method. The OAM multiplexer based on the MPLC method realizes its mode conversion function by using multiple phase planes, and the phase distribution of the phase plane can be calculated using the wavefront-matching algorithm. Wavefront matching means that forward-propagating light fields should be matched with backward-propagating light fields at any position in the space. In the wavefront-matching algorithm, the phase distribution of the phase plane Φ is equal to the superposition of the conjugate input light field (I^*) of N separate channels and the output light field (O) of N orders in the phase plane:

$$\Phi = \arg\left\{\sum_{i=1}^{N} I^* \cdot O\right\}. \tag{1}$$

The input light field and the output light field can be determined by using the angular spectrum algorithm. The phase plane is updated, and the iterative calculation involved is repeated until the algorithm converges to provide the phase distribution of the phase plane.

Figure 1(a) shows a schematic of the OAM multiplexer based on inversely-designed MPLC. The inverse-design process is sensitive to the initial value of the phase mask and is oriented via algorithm optimization. We establish our optimization objective function by determining the best conversion efficiency for the light field that is given by the overlapping integral between the generated mode and the ideal mode $|\langle\phi_k^{\text{output}}|\phi_k^{\text{ideal}}\rangle|^2$ and the crosstalk between the light fields $|\langle\phi_k^{\text{output}}|\phi_{k'}^{\text{ideal}}\rangle|^2$, where ϕ_k^{output} represents the output spatial mode with a mode index of k, and $\phi_{k'}^{\text{ideal}}$ is the ideal spatial mode with a mode index of k'. Figure 1(b) shows the MPLC optimization flowchart. The above is combined with the particle swarm optimization algorithm to find the optimal solution for the design, including (1) the beam waist diameter of the input Gaussian beam, (2) the input fiber array pitches, (3) the number of phase planes (P1, P2, P3, P4, P5), (4) the distance between the light source and the first phase plane, (5) the spacing arrangement for the phase planes, and (6) the diameter of the output beam. The search parameters are updated during the iterative process to calculate the objective optimization function value, and, each time the objective optimization function is improved, the new parameter value is recorded. To escape from the local optimal solution in the design, the mask obtained in each design iteration can be used as the initial value for the next iteration to optimize the parameter search again. We found that there was no need to gain the best value from the first iteration because the design process is initially conducted based on a mask, and we gained better value from performing several iteration processes.

The phase mask is composed of five phase planes, each of which has dimensions of 4.8 mm × 4.8 mm. The phase profiles for the five inversely-designed phase planes are shown in Fig. 1(c). After the optimization, we found that the phase plate P1 is acting as an element superimposing a cylindrical lens phase and a grating gradient phase. The phase of P2 is employed to compensate the grating gradient phase of the light field after the light passes through the first phase plane. The phase of P3 is acting as a phase corrector. Finally, P4 and P5 are used as beam combiner converters to realize the transformation from the strip light spots to the doughnut shapes of OAM. The phase optimization process shows that the algorithm has assisted to find a better optical field evolution path from the Gaussian spots to the OAM beams and thus realize efficient mode transformation. The devices that were manufactured on a silicon wafer via three cycles of photolithography and etching are illustrated in Fig. 1(d); the fabrication procedures are shown in Appendix A. The fabricated phase masks are reflective devices with eight phase levels ranging between 0 and

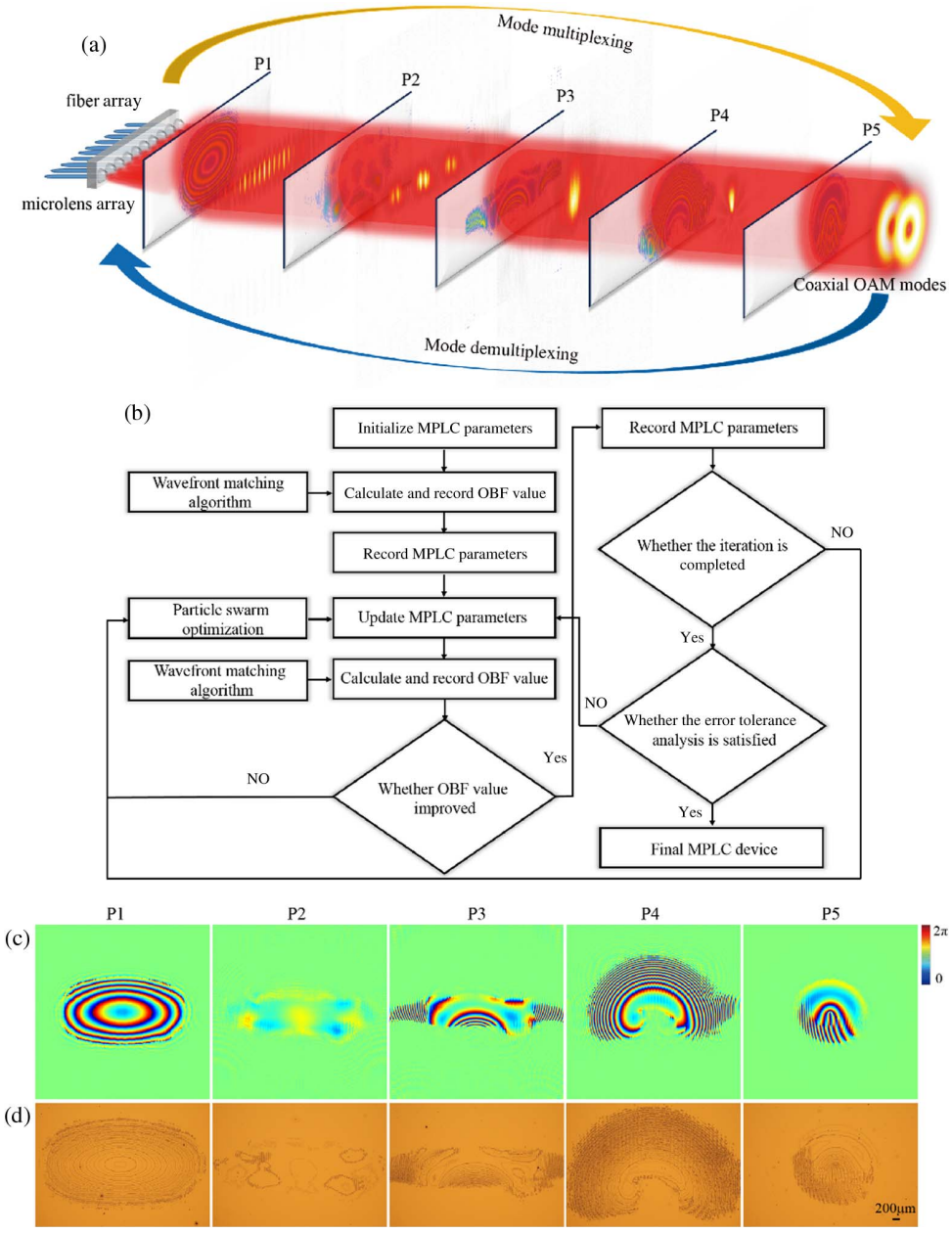

Fig. 1. OAM mode transformation via an inversely-designed multiphase plane light conversion. (a) Multiphase planes are designed to perform reversible mode conversion between multiple axial OAM modes and a Gaussian spot array. (b) MPLC optimization flowchart; OBF, optimization objective function. (c) Phase distributions for the five designed phase planes. (d) Corresponding microscopic images of the fabricated devices.

2π at 1550 nm, corresponding to etching depths between 0 and 775 nm. The surfaces of the phase masks are then coated with 110 nm gold layers to improve their reflectivity. The pixel size of the phase mask is 8 μm. To achieve the purpose of generating center coaxial modes, the input Gaussian light located farther from the center requires a more dramatic phase gradient to change its diffraction angle during propagation than that at the central incident spot.

3. EXPERIMENTAL RESULTS AND ANALYSIS

The reflective OAM multiplexer is shown in Fig. 2(a), where the phase mask for the OAM (de)multiplexer contains five phase planes. The fiber array and the microlens array output 11 collimated Gaussian beams that pass through five phase planes accurately by adjusting the phase mask and the mirror [49]. The pitch for the fiber array and the microlens array is 250 μm. The distance between the light source and the first phase plane is 44 mm; the distance between adjacent phase planes is 70 mm. The waist diameter of the input beam is 110 μm; the waist diameter of the output beam is 400 μm. The 11 Gaussian beams are input into different positions in the OAM multiplexer and converted into the −5th to 5th orders of OAM for coaxial transmission. The insertion losses of the OAM from the −5th to 5th orders are less than 2.6 dB,

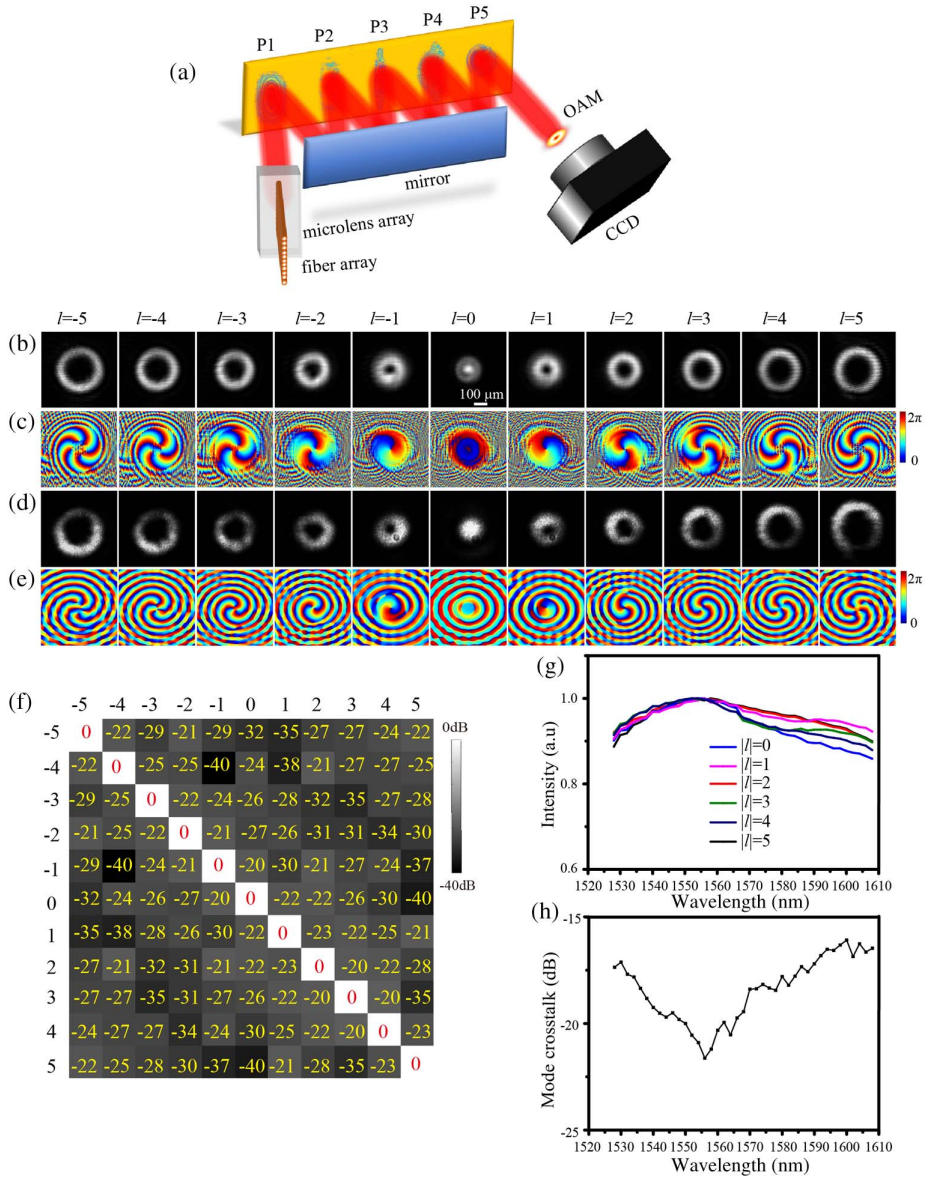

Fig. 2. (a) Reflective OAM multiplexer based on MPLC. Calculated images of (b) the OAM intensity profile and (c) the phase of the OAM. (d) Intensity profiles of the OAM generated by MPLC in the experiments. (e) Reconstructed phase profiles for the OAM generated from off-axis holography. (f) Measured mode crosstalk matrix for the OAM. (g) Conversion efficiency and (h) maximum mode crosstalk of the OAM multiplexer over the C-band and the L-band wavelengths.

including the phase mask, mirror, and mode conversion losses. Here, the insertion loss is defined as

$$\mathrm{IL} = 10\log\frac{P_{\mathrm{out}}}{P_{\mathrm{in}}}, \tag{2}$$

where P_{out} is the measured output power of the generated OAM mode, and P_{in} is the power of the incident Gaussian beam. Figures 2(b) and 2(c) show the numerical simulation results for the intensity profiles and the phases of the generated coaxial OAM with topological charges ranging from −5th to 5th, respectively. In the experiments, the intensity profiles of the generated OAM were captured directly using an infrared charge-coupled device (CCD) [Fig. 2(d)]. From the intensity profiles of the generated OAM, we find that the size of the ring increases when the OAM topological charge increases. However, the phase profile of the OAM is difficult to measure directly during the experiment. Therefore, we reconstructed the OAM phase in the experiment via off-axis holography (see Appendix B). Figure 2(e) shows the phase of the OAM restored using off-axis holography. It is observed from the OAM phase that the number of rotating fringes is equal to the number of topological charges of OAM, the positive-order OAM rotates counterclockwise; the negative-order OAM rotates clockwise. These experimental results are basically consistent with the calculated results.

The measured phases of the OAM are consistent with the calculated phases of the OAM. By a process of correlation of all the generated OAM, we extracted the OAM crosstalk matrix,

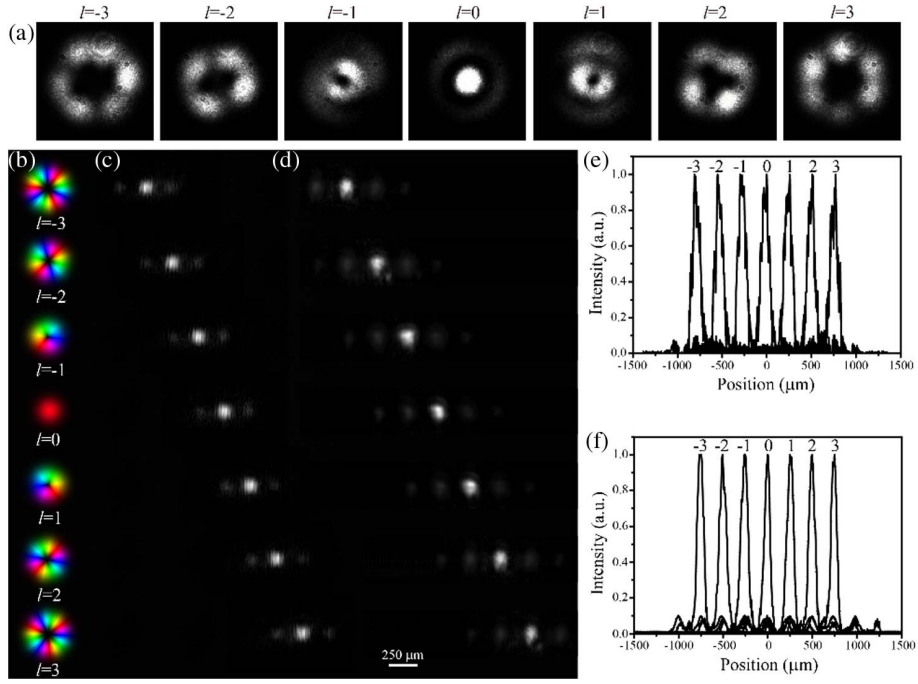

Fig. 3. (a) OAM generated by MPLC is transmitted in few-mode fiber. (b) Input OAM from −3rd to 3rd orders. (c) Calculated OAM sorting results with displacements proportional to the incident OAM order. (d) Experimental results of OAM sorting as captured using an infrared camera. (e) Calculated and (f) measured sorting results for intensity distributions with orders ranging from −3rd to +3rd.

as shown in Fig. 2(f). The mode crosstalk of the OAM generated by MPLC is less than −20 dB and is mainly generated by imperfect fabrication and misalignment during the experiment. The crosstalk between OAM modes with the topological charges m and n is defined as

$$\text{Crosstalk}_{n,m} = 10 \cdot \log\left(\frac{P_n}{P_m}\right), \tag{3}$$

where P_m is the measured output power of the designed target mode, and P_n is the measured output power of the unwanted mode. Use of a phase mask for MPLC with more phase levels can further reduce the mode crosstalk of the OAM. Error tolerance determines that MPLC can be used in broadband. We observed the conversion efficiency of the OAM multiplexer at different wavelengths. These wavelengths covered the C-band and the L-band, as shown in Fig. 2(g). The disparity among the conversion efficiencies of OAM multiplexers operating at different wavelengths is less than 20%. We also measured the mode crosstalk at C-band and the L-band for the OAM generated by the multiplexer; the maximum mode crosstalk is shown in Fig. 2(h). The mode crosstalk varies by 4.5 dB between the C-band and the L-band wavelengths. Therefore, the proposed OAM multiplexer based on inversely-designed MPLC is a wide-bandwidth photonic device.

MPLC can also be used in OAM demultiplexing. The MPLC technique based on inverse design must design the phase plane according to the incident beam waist diameter, which places strict requirements on the incident beam. Few mode fibers can be encapsulated in a graded index lens (G-lens) and control the beam waist diameter based on the focal length of G-lens. Therefore, the OAM generated by the OAM multiplexer is coupled to the few-mode fiber via a G-lens, and the total system loss is less than 12 dB. The commercial few-mode fiber used is a step-type fiber with a core diameter of 16 μm that supports OAM transmission from the −3rd to +3rd orders. We demonstrate the OAM with topology from −3rd to 3rd generated by MPLC is transmitted in a few-mode fiber. The OAM output from a 5 km few-mode fiber is shown in Fig. 3(a). The OAM output from the G-lens can then be sorted by MPLC. Limited by the commercial few-mode fibers that were available, we only demonstrated OAM sorting from the −3rd to +3rd orders of OAM. Figure 3(b) shows the incident OAM from the −3rd to +3rd orders. The order of the OAM is equal to the number of 0–2π phase changes, and the positive and negative orders represent the directions of these phase changes. The incident OAM is converted into a Gaussian beam by passing through the P5, P4, P3, P2, and P1 phase planes in sequence. The calculated OAM sorting result is a Gaussian spot that has a displacement proportional to the incident OAM order, as shown in Fig. 3(c). The light spots shown are Gaussian spots, which are suitable for free-space-to-fiber coupling. Using the zeroth-order OAM as a reference, the positive (negative) OAM orders are offset toward the right (left). The experimental results of OAM sorting are consistent with the calculated results, as shown in Fig. 3(d). There is some crosstalk on both sides of the sorted results. We extracted the intensity distributions of the sorting spots from computational and experimental images. Figures 3(e) and 3(f) show the calculated and measured intensity distributions, respectively, of the OAM sorting results from the −3rd order to the +3rd order. The distance between the adjacent Gaussian spots is 250 μm, which matches the fiber array dimensions. We couple

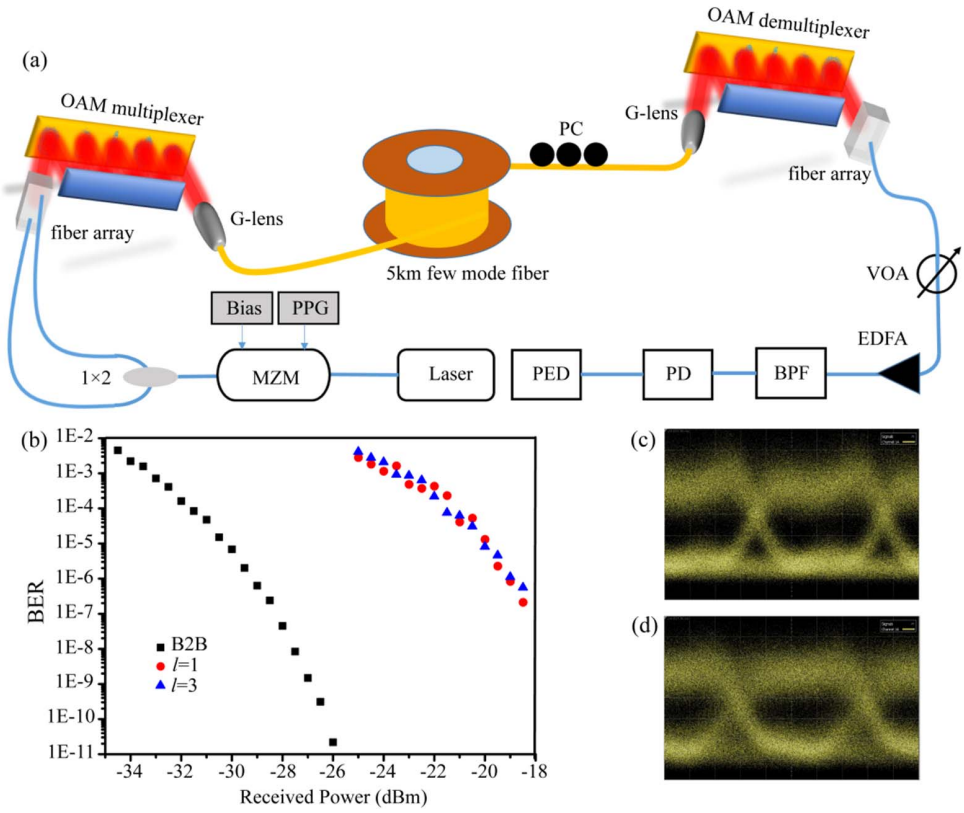

Fig. 4. (a) Experimental setup for OAM multiplexing-based fiber communication using MPLC; PPG, programmable pulse generator; MZM, Mach–Zehnder modulator; PC, polarization controller; VOA, variable optical attenuator; EDFA, erbium-doped fiber amplifier; BPF, bandpass filter; PD, photodetector; PED, programmable error detector. (b) Measured BERs of the multiplexed coaxial OAM mode channels in 5 km few-mode fiber communications; eye diagrams of OAM for (c) $l = 1$ and (d) $l = 3$.

the Gaussian spots to a single-mode fiber array through a microlens array with total system loss of less than 14 dB. Further, the power meter detection shows that the crosstalk of the different orders of the OAM is less than −10 dB. Crosstalk and large insertion loss are caused by side lobes. The side lobes in the sorted OAM beams come from the high-order diffraction properties of the devices.

In this work, we have demonstrated OAM multiplexing communication based on two MPLC devices, where one was used as an OAM multiplexer and the other used as an OAM demultiplexer. Figure 4(a) shows the experimental setup for OAM multiplexing-based fiber communication using MPLC. A 1550 nm laser beam is modulated to carry a 10 Gbit/s on–off keying signal from a pattern generator; this beam is then split into two branches using a coupler. Two channels are then converted to produce coaxial OAM via an OAM multiplexer. The G-lens couples the coaxial OAM to a few-mode fiber for transmission over 5 km. The coaxial OAM is incident on the OAM demultiplexer from the G-lens at the other end of the few-mode fiber. The polarization controller is then adjusted carefully to ensure that the OAM is demultiplexed sufficiently. The coaxial OAM demultiplexing results are coupled into a single-mode fiber array for BER testing. Figure 4(b) shows the BER of coaxial OAM communication in 5 km few-mode fiber with the power penalties less than 10 dB. The BER curve illustrates that the OAM (de)multiplexer based on MPLC is suitable for use in optical fiber communications. Figures 4(c) and 4(d) show the eye diagrams for the OAM topological charges of 1 and 3, respectively. The eye diagrams for two OAM channels are both with clear opens and small slopes, which indicate the excellent performance of MPLC in OAM multiplexed communication. The big opens show the good signal-to-noise ratio, and the crossings illustrate the small jitter of the signal. The similarity between the two diagrams indicates a consistent good performance of MPLC device over all the multiplexing OAM channels.

4. CONCLUSION

In summary, we have proposed and experimentally demonstrated an OAM mode (de)multiplexer based on inversely-designed MPLC. The proposed device is shown to be a good OAM mode multiplexer and a good mode sorter. After passing through the five phase planes, the coaxial OAM modes can be transferred smoothly into spatially separated Gaussian beams and vice versa. The mode (de)multiplexing process shows an insertion loss of less than 2.6 dB and mode crosstalk less than −20 dB. Additionally, the proposed device is also a broadband device and works well over the C-band and the L-band range, which demonstrates a considerable advantage when compared with conventional OAM (de)multiplexing devices. In the OAM mode multiplexing communication experiment,

the OAM (de)multiplexer demonstrates high performance. More importantly, the proposed inverse design method is general and can be used in multidimensional multiplexing, e.g., for a mode and wavelength-based hybrid multiplexer.

APPENDIX A: MPLC DEVICE FABRICATION

The optimized five phase planes [P1, P2, P3, P4, and P5 in Fig. 1(c)] are designed for a wavelength at 1550 nm. The corresponding phase delay Φ is transferred to a reflection distance that is related to the etching depth on the silicon wafer as $h = \frac{\Phi\lambda}{4\pi}$. For the convenience of fabrication, the etching depth h is discretized as eight-level, which can be easily realized through a three-step UV mask aligner lithography. For a reflector at 1550 nm, an etching depth of 775 nm corresponds to a 2π phase delay. Dividing 775 nm into eight steps, then each etching step is 97 nm. The phase diagram is converted into matrix of 0 to 8 corresponding to a 3 bit binary number. Each bit of the three-digit binary number corresponds to a mask. The corresponding etching depth of the first mask is 388 nm, the etching depth of the second mask is 194 nm, and the etching depth of the third mask is 97 nm. The fabrication procedure is illustrated in Fig. 5. A thin layer of UV photoresist is spin-coated on a silicon wafer; then, the silicon wafer covered with first mask is exposed under UV light. After development, the silicon wafer is etched to a depth of 388 nm. Then, the silicon wafer is cleaned, and the UV photoresist is spin-coated to perform the second lithography with the second mask; the corresponding etching depth is 194 nm. Repeat the above steps and then expose the third mask to a corresponding etching depth of 97 nm. The surface of the fabricated silicon wafer is then coated with 110 nm gold to improve the reflectivity.

APPENDIX B: OFF-AXIS HOLOGRAPHIC RECONSTRUCTION OF OAM PHASE

In the experiment, we reconstructed the amplitude and phase of the OAM mode profile generated by the device using an off-axis digital holography [Fig. 6(a)]. After the beam is generated from the laser, the optical fiber is divided into a signal arm and a reference arm, which is adjusted by two polarization controllers to achieve consistent polarization. The beam splitter is used to combine the beam coherence, and the infrared camera is used to capture the interference image [Fig. 6(b)]. The amplitude and phase information of the OAM beam is recorded in the interferogram. The −1st, +1st, and 0th orders can be separated

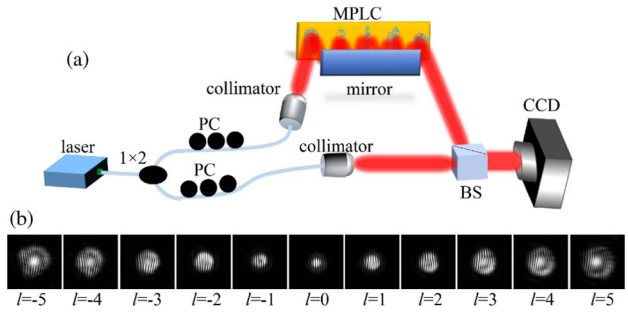

Fig. 6. Characterization apparatus of MPLC. (a) Setup of MPLC off-axis digital holography. (b) Interference pattern of OAM.

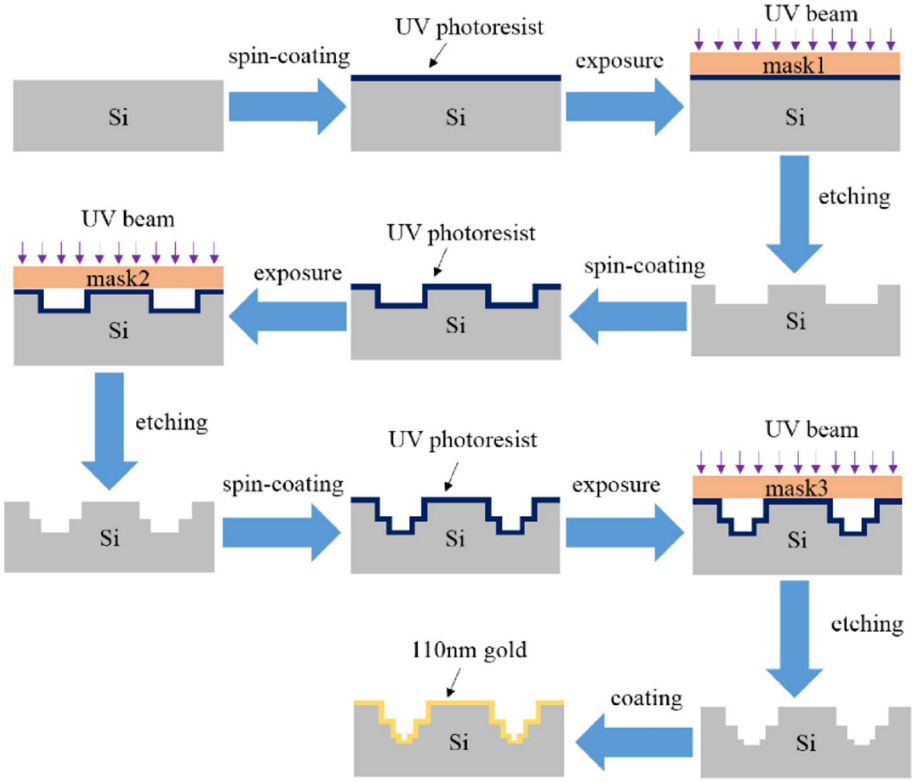

Fig. 5. MPLC device fabrication procedure.

by a Fourier transform of the obtained interference image. The amplitude and phase of the light field can be recovered by an inverse Fourier transform. By restoring the intensity and phase information of all modes, we can obtain the transmission matrix of the device.

By the correlation among all the generated OAM, we extract the OAM crosstalk matrix for the OAM as shown in Fig. 2(f). The mode crosstalk of OAM generated by MPLC is lower than −20 dB, mainly from the imperfect fabrication and misalignment in the experiment.

Funding. National Key Research and Development Program of China (2018YFB1801801); Guangdong Major Project of Basic Research (2020B0301030009); National Natural Science Foundation of China (61935013, 61975133, 62075139, 61705135, 12047540, 62175162, 62105215); Natural Science Foundation of Guangdong Province (2020A1515011185); Science, Technology and Innovation Commission of Shenzhen Municipality (RCJC20200714114435063, KQJSCX20170727100838364, JCYJ20180507182035270, JCYJ20200109114018750); Shenzhen Peacock Plan (KQTD20170330110444030); Shenzhen University (2019075).

Acknowledgment. The authors would like to acknowledge the Photonics Center of Shenzhen University for providing technical support.

Disclosures. The authors declare no conflicts of interest.

Data Availability. Data underlying the results presented in this paper are not publicly available at this time but may be obtained from the authors upon reasonable request.

[†]These authors contributed equally to this paper.

REFERENCES

1. L. Allen, M. W. Beijersbergen, R. J. C. Spreeuw, and J. P. Woerdman, "Orbital angular momentum of light and the transformation of Laguerre-Gaussian laser modes," Phys. Rev. A **45**, 8185–8189 (1992).
2. M. Padgett, J. Arlt, and N. Simpson, "An experiment to observe the intensity and phase structure of Laguerre-Gaussian laser modes," Am. J. Phys. **64**, 77–82 (1996).
3. B. Spektor, A. Normatov, and J. Shamir, "Singular beam microscopy," Appl. Opt. **47**, A78–A87 (2008).
4. J. Masajada, M. Leniec, E. Jankowska, H. Thienpont, H. Ottevaere, and V. Gomez, "Deep microstructure topography characterization with optical vortex interferometer," Opt. Express **16**, 19179–19191 (2008).
5. I. Gianani, A. Suprano, T. Giordani, N. Spagnolo, F. Sciarrino, D. Gorpas, V. Ntziachristos, K. Pinker, N. Biton, and J. Kupferman, "Transmission of vector vortex beams in dispersive media," Adv. Photon. **2**, 036003 (2020).
6. M. P. Lavery, F. C. Speirits, S. M. Barnett, and M. J. Padgett, "Detection of a spinning object using light's orbital angular momentum," Science **341**, 537–540 (2013).
7. W. Wang, T. Yokozeki, R. Ishijima, A. Wada, Y. Miyamoto, M. Takeda, and S. G. Hanson, "Optical vortex metrology for nanometric speckle displacement measurement," Opt. Express **14**, 120–127 (2006).
8. D. G. Grier, "A revolution in optical manipulation," Nature **424**, 810–816 (2003).
9. E. Otte and C. Denz, "Optical trapping gets structure: structured light for advanced optical manipulation," Appl. Phys. Rev. **7**, 041308 (2020).
10. D. Mao, Y. Zheng, C. Zeng, H. Lu, C. Wang, H. Zhang, W. D. Zhang, T. Mei, and J. L. Zhao, "Generation of polarization and phase singular beams in fibers and fiber lasers," Adv. Photon. **3**, 014002 (2021).
11. R. Fickler, R. Lapkiewicz, W. N. Plick, M. Krenn, C. Schaeff, S. Ramelow, and A. Zeilinger, "Quantum entanglement of high angular momenta," Science **338**, 640–643 (2012).
12. J. C. Garcia-Escartin and P. Chamorro-Posada, "Quantum multiplexing with the orbital angular momentum of light," Phys. Rev. A **78**, 5175–5179 (2008).
13. A. Nicolas, L. Veissier, L. Giner, E. Giacobino, D. Maxein, and J. Laurat, "A quantum memory for orbital angular momentum photonic qubits," Nat. Photonics **8**, 234–238 (2014).
14. X. L. Wang, X. D. Cai, Z. E. Su, M. C. Chen, D. Wu, L. Li, N. L. Liu, C. Y. Lu, and J. W. Pan, "Quantum teleportation of multiple degrees of freedom of a single photon," Nature **518**, 516–519 (2015).
15. D. Cozzolino, E. Polino, M. Valeri, G. Carvacho, D. Bacco, N. Spagnolo, L. K. Oxenlowe, and F. Sciarrino, "Air-core fiber distribution of hybrid vector vortex-polarization entangled states," Adv. Photon. **1**, 046005 (2019).
16. J. Wang, "Advances in communications using optical vortices," Photon. Res. **4**, B14–B28 (2016).
17. S. Yu, "Potentials and challenges of using orbital angular momentum communications in optical interconnects," Opt. Express **23**, 3075–3087 (2015).
18. A. M. Yao and M. J. Padgett, "Orbital angular momentum: origins, behavior and applications," Adv. Opt. Photon. **3**, 161–204 (2011).
19. X. Y. Fang, H. C. Yang, W. Z. Yao, T. X. Wang, Y. Zhang, M. Gu, and M. Xiao, "High-dimensional orbital angular momentum multiplexing nonlinear holography," Adv. Photon. **3**, 015001 (2021).
20. Y. J. Shen, X. J. Wang, Z. W. Xie, C. J. Min, X. Fu, Q. Liu, M. L. Gong, and X. C. Yuan, "Optical vortices 30 years on: OAM manipulation from topological charge to multiple singularities," Light Sci. Appl. **8**, 90 (2019).
21. J. Wang, J. Y. Yang, I. M. Fazal, N. Ahmed, Y. Yan, H. Huang, Y. X. Ren, Y. Yue, S. Dolinar, M. Tur, and A. E. Willner, "Terabit free-space data transmission employing orbital angular momentum multiplexing," Nat. Photonics **6**, 488–496 (2012).
22. N. Bozinovic, Y. Yue, Y. Ren, M. Tur, P. Kristensen, H. Huang, A. E. Willner, and S. Ramachandran, "Terabit-scale orbital angular momentum mode division multiplexing in fibers," Science **340**, 1545–1548 (2013).
23. A. Forbes, A. Dudley, and M. McLaren, "Creation and detection of optical modes with spatial light modulators," Adv. Opt. Photon. **8**, 200–227 (2016).
24. M. W. Beijersbergen, R. P. C. Coerwinkel, M. Kristensen, and J. P. Woerdman, "Helical-wavefront laser beams produced with a spiral phaseplate," Opt. Commun. **112**, 321–327 (1994).
25. Y. M. Li, J. Kim, and M. J. Escuti, "Orbital angular momentum generation and mode transformation with high efficiency using forked polarization gratings," Appl. Opt. **51**, 8236–8245 (2012).
26. T. Lei, M. Zhang, Y. Li, P. Jia, G. N. Liu, X. Xu, Z. Li, C. Min, J. Lin, C. Yu, H. Niu, and X. Yuan, "Massive individual orbital angular momentum channels for multiplexing enabled by Dammann gratings," Light Sci. Appl. **4**, e257 (2015).
27. Z. Xie, S. Gao, T. Lei, S. Feng, Y. Zhang, F. Li, J. Zhang, Z. Li, and X. Yuan, "Integrated (de)multiplexer for orbital angular momentum fiber communication," Photon. Res. **6**, 743–749 (2018).
28. J. Leach, J. Courtial, K. Skeldon, S. M. Barnett, S. Franke-Arnold, and M. J. Padgett, "Interferometric methods to measure orbital and spin, or the total angular momentum of a single photon," Phys. Rev. Lett. **92**, 013601 (2004).
29. G. C. G. Berkhout, M. P. J. Lavery, J. Courtial, M. W. Beijersbergen, and M. J. Padgett, "Efficient sorting of orbital angular momentum states of light," Phys. Rev. Lett. **105**, 153601 (2010).
30. M. P. J. Lavery, G. C. G. Berkhout, J. Courtial, and M. J. Padgett, "Measurement of the light orbital angular momentum spectrum using an optical geometric transformation," J. Opt. **13**, 064006 (2011).
31. M. Mirhosseini, M. Malik, Z. Shi, and R. W. Boyd, "Efficient separation of the orbital angular momentum eigenstates of light," Nat. Commun. **4**, 2781 (2013).

32. G. Ruffato, M. Massari, and F. Romanato, "Multiplication and division of the orbital angular momentum of light with diffractive transformation optics," Light Sci. Appl. **8**, 113 (2019).
33. B. Wang, Y. H. Wen, J. B. Zhu, Y. J. Chen, and S. Y. Yu, "Sorting full angular momentum states with Pancharatnam-Berry metasurfaces based on spiral transformation," Opt. Express **28**, 16342–16351 (2020).
34. Y. Wen, I. Chremmos, Y. Chen, J. Zhu, Y. Zhang, and S. Yu, "Spiral transformation for high-resolution and efficient sorting of optical vortex modes," Phys. Rev. Lett. **120**, 193904 (2018).
35. Y. Wen, I. Chremmos, Y. Chen, G. Zhu, J. Zhang, J. Zhu, Y. Zhang, J. Liu, and S. Yu, "Compact and high-performance vortex mode sorter for multi-dimensional multiplexed fiber communication systems," Optica **7**, 254–262 (2020).
36. N. F. Yu, P. Genevet, M. A. Kats, F. Aieta, J. P. Tetienne, F. Capasso, and Z. Gaburro, "Light propagation with phase discontinuities: generalized laws of reflection and refraction," Science **334**, 333–337 (2011).
37. S. Chen, Y. Cai, G. X. Li, S. Zhang, and K. W. Cheah, "Geometric metasurface fork gratings for vortex-beam generation and manipulation," Laser Photon. Rev. **10**, 322–326 (2016).
38. H. Ren, X. P. Li, Q. M. Zhang, and M. Gu, "On-chip noninterference angular momentum multiplexing of broadband light," Science **352**, 805–809 (2016).
39. F. Feng, G. Y. Si, C. J. Min, X. C. Yuan, and M. G. Somekh, "On-chip plasmonic spin-Hall nanograting for simultaneously detecting phase and polarization singularities," Light Sci. Appl. **9**, 95 (2020).
40. Y. Guo, S. C. Zhang, M. B. Pu, Q. He, J. J. Jin, M. F. Xu, Y. X. Zhang, P. Gao, and X. G. Luo, "Spin-decoupled metasurface for simultaneous detection of spin and orbital angular momenta via momentum transformation," Light Sci. Appl. **10**, 63 (2021).
41. Z. Xie, T. Lei, G. Y. Si, L. P. Du, J. Lin, C. J. Min, and X. C. Yuan, "On-chip spin-controlled orbital angular momentum directional coupling," J. Phys. D **51**, 0140021 (2017).
42. N. Zhou, S. Zheng, X. P. Cao, Y. F. Zhao, S. Q. Gao, Y. T. Zhu, M. B. He, X. L. Cai, and J. Wang, "Ultra-compact broadband polarization diversity orbital angular momentum generator with 3.6×3.6 mm^2 footprint," Sci. Adv. **5**, eaau9593 (2019).
43. Z. W. Xie, T. Lei, F. Li, H. D. Qiu, Z. C. Zhang, H. Wang, C. J. Min, L. P. Du, Z. H. Li, and X. C. Yuan, "Ultra-broadband on-chip twisted light emitter for optical communications," Light Sci. Appl. **7**, 18001 (2018).
44. G. Labroille, B. Denolle, P. Jian, P. Genevaux, N. Treps, and J. F. Morizur, "Efficient and mode selective spatial mode multiplexer based on multi-plane light conversion," Opt. Express **22**, 15599–15607 (2014).
45. G. Ruffato, V. Grillo, and F. Romanato, "Multipole-phase division multiplexing," Opt. Express **29**, 38095–38108 (2021).
46. L. He, Z. Lin, Y. Wen, Y. Chen, and S. Yu, "An inverse design method combining particle swarm optimization and wavefront matching method for multiplane light conversion," in *Frontiers in Optics 2020/Laser Science* (Optical Society of America, 2020), paper FM7D.5.
47. N. K. Fontaine, R. Ryf, H. Chen, D. T. Neilson, K. Kim, and J. Carpenter, "Laguerre-Gaussian mode sorter," Nat. Commun. **10**, 1865 (2019).
48. H. Wen, Y. H. Zhang, R. Sampson, N. K. Fontaine, N. Wang, S. L. Fan, and G. F. Li, "Scalable non-mode selective Hermite-Gaussian mode multiplexer based on multi-plane light conversion," Photon. Res. **9**, 88–97 (2021).
49. J. C. Fang, J. Bu, J. P. Li, C. X. Lin, A. Kong, X. Yin, H. Luo, X. Song, Z. Xie, T. Lei, and X. Yuan, "Performance optimization of multi-plane light conversion (MPLC) mode multiplexer by error tolerance analysis," Opt. Express **29**, 37852–37861 (2021).
50. T. Yan, J. M. Wu, T. K. Zhou, H. Xie, F. Xu, J. T. Fan, L. Fang, X. Lin, and Q. H. Dai, "Fourier-space diffractive deep neural network," Phys. Rev. Lett. **123**, 023901 (2019).
51. S. Zheng, S. Xu, and D. Fan, "Orthogonality of diffractive deep neural network," Opt. Lett. **47**, 1798–1801 (2022).
52. X. Lin, Y. Rivenson, N. T. Yardimei, M. Veli, Y. Luo, M. Jarrahi, and A. Ozcan, "All-optical machine learning using diffractive deep neural networks," Science **361**, 1004–1008 (2018).
53. T. Giordani, A. Suprano, E. Polino, F. Acanfora, L. Innocenti, A. Ferraro, M. Paternostro, N. Spagnolo, and F. Sciarrino, "Machine learning-based classification of vector vortex beams," Phys. Rev. Lett. **124**, 160401 (2020).